Mineralogical and geochemical composition of a cementitious grout and its evolution during interaction with water

Sylvain Grangeon, Mathieu Debure, Valerie Montouillout, Erik Elkaim, Catherine Lerouge, Nicolas Maubec, Nicolas Michau, Xavier Bourbon, Christelle Martin, Benoit Cochepin, et al.

npj | materials degradation

Article

Published in partnership with CSCP and USTB

https://doi.org/10.1038/s41529-024-00488-0

Mineralogical and geochemical composition of a cementitious grout and its evolution during interaction with water

Sylvain Grangeon[1] ✉, Mathieu Debure[1] ✉, Valerie Montouillout[2], Erik Elkaim[3], Catherine Lerouge[1], Nicolas Maubec[1], Nicolas Michau[4], Xavier Bourbon[4], Christelle Martin[4], Benoit Cochepin[4] & Nicolas Marty[1]

In the present study, the chemical composition, mineralogy, and mechanisms of alteration of a cementitious grout based on a CEM III/C with addition of smectite, hydrotalcite, and silica fume, are studied using a combination of chemical and physical methods. This material was designed in the context of geological repository of radioactive wastes, with a twofold aim: first, to fill the technical voids left by drilling operations at the interface between the geological formation and the disposal galleries. Second, to neutralize a potential acidic transient due to pyrite oxidation, and to create an environment that favors low corrosion rates of carbon steels. The grout is mainly composed of calcium silicate hydrates having a Ca/Si ratio of ~0.8, incorporating Al in the bridging site of the Si chains (C-A-S-H), and accounting for 29–36 wt.% of the sample. It also contains silica fume (38–48 wt.%), smectite with interlayer Na (11–17 wt.%), hydrotalcite with interlayer CO_3^{2-} (3–4 wt.%), and lower amounts of portlandite, calcite, and possibly gibbsite and gypsum. Upon alteration by water in a flow-through reactor, the main modifications affecting the sample are calcite and gypsum dissolution, hence releasing aqueous Ca^{2+} that is adsorbed in smectite interlayer by replacing Na^{+}, and stoichiometric C-A-S-H dissolution. The evolution of solution chemistry and of the solid phase composition are reproduced successfully using a thermokinetic model.

In France, intermediate-level long-lived waste and high-level waste are foreseen to be disposed in a deep underground geological repository, within a clayey formation from the Callovian-Oxfordian age. In the design under study, the vitrified waste is poured in a stainless steel container, itself put in a carbon steel overpack to facilitate handling and to avoid exposing the glass to water while temperature is above 50 °C. The whole assembly is slid into a carbon steel casing. A detailed description of the disposal concept and in particular of the different barriers protecting the waste can be found in a publication by Diler et al.[1]. During the drilling operations in such clayey formations, the formation of an excavation damaged (fractured) zone that extends from the drilled zone to a few tens of centimetres in the clayey rock cannot be avoided. Fractures lead to partial rock desaturation and potentially to oxygen diffusion, which in turn oxidizes pyrite contained in the clayey rock. The empty space left in between the clayey rock and the carbon steel liner favors such mineral and chemical changes. Pyrite oxidation is accompanied by pore water acidification. This acidification is buffered by dissolution of carbonate minerals (mainly calcite) contained in the clay rock. This leads to production of CO_2 in the disposal galeries[2,3] and potentially transitory pH decrease. Both pore water acidification and presence of O_2 are susceptible to react with the engineered structures, and in particular with the carbon steel. To limit these unwanted chemical reactions, Andra (French national radioactive waste management agency) has been developing a cementitious grout, with the objective of filling the technical voids left between the carbon steel casing and fractured host rock[4]. This material must fulfill several requirements. This includes: to provide a pH neutralization capacity during the operation period, a pore water pH ranging between 9.5 and 12.5, a pH after neutralization of the acidic plume close to 9.5, a Mg content close to that of the Callovian-Oxfordian clayey rock, no residual alkaline reserve to avoid enhanced glass corrosion, and negligible content of organic species[5]. The material must also have a good injectability[5].

Goethals et al.[6] previously investigated the interaction of a cementitious grout with carbon steel, under anoxic and spatially heterogeneous conditions, and at 80 °C, with the cementitious grout having a different composition than the one studied here (based on a 600/600/160/40 mass ratio of CEM III/A/

[1]BRGM, F-45060 Orléans, France. [2]Conditions Extrêmes et Matériaux: Haute Température et Irradiation (CEMHTI), CNRS UPR 3079, 1D Avenue de la Recherche Scientifique, 45071 Orléans, France. [3]Synchrotron SOLEIL, L'Orme des Merisiers, 91190 Saint-Aubin, France. [4]Andra, 1/7 Rue Jean Monnet, 92290 Châtenay-Malabry, France. ✉e-mail: s.grangeon@brgm.fr; m.debure@brgm.fr

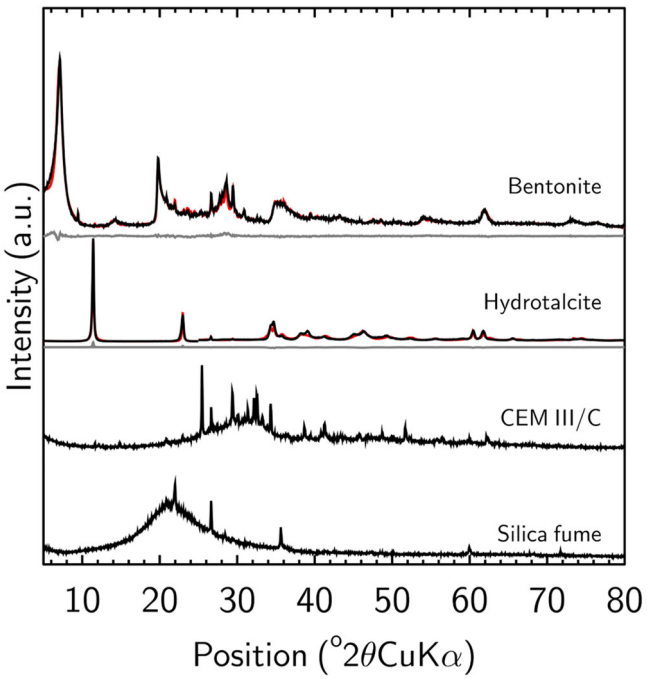

Fig. 1 | Experimental (black solid line) and modeled (red solid line) XRD patterns of, from top to bottom, bentonite, hydrotalcite, CEM III/C, and silica fume. Intensity scale multiplied by 5 for the 25–80 °2θ interval as compared to the 5–25 °2θ interval for the hydrotalcite patterns. The gray solid line below bentonite and hydrotalcite patterns are the difference between experimental and modeled patterns.

Silica fume/Bentonite/Hydrotalcite). The interaction induced the formation of corrosion pits measuring up to 160 µm after 147 days of interaction at 80 °C, and the corrosion rate dropped after 1 year of interaction, indicating potential passivation. The corrosion led to the formation of magnetite, with further transformation to Fe-silicates and Fe-sulfides. This evolution was attributed to the presence of HS^- and residual O_2 in the cementitious grout. In addition, a preferential release of Ca and dissolution of the silica fume from the cementitious grout was observed at the cathodic zone, leading to interaction between Fe and calcium silicate hydrates (C-S-H in cement nomenclature). Overall, this study highlighted the need to quantify the mineralogy and geochemistry of the cementitious grout to allow for a sound thermo-kinetic modeling of the cementitious grout reactivity and of its evolution with time. Indeed, during the operation period, the pore water diffusion through the cementitious grout will induce a number of dissolution, recrystallization, and (or) precipitation reactions. Ensuring the medium-term performance during this period and knowing the long-term behavior of this material after closure of the repository requires that the geochemical and mineralogical evolution, including reaction kinetics, can be predicted with a high degree of confidence. Such knowledge can be gained from a sound description of the mineralogy and geochemistry of the filling material and from the analysis and modeling of its mineralogical and geochemical evolution in response to geochemical perturbations. Here, we characterized the mineralogy and geochemistry of a specifically designed cementitious grout, previously investigated for its evolution as a function of temperature[5] and its influence on microbially-influenced steel corrosion[1]. By combining several laboratory and synchrotron experiments, we quantified and modeled its in situ mineralogical and geochemical evolution during its alteration by water. This allowed developing a geochemical model, based on a sound understanding of the mineralogy, which will be valuable for the prediction of the long-term fate of this cementitious grout, in particular in the context of geological waste disposal. Since this cementitious grout was mainly composed of cement phases (e.g., calcium silicate hydrates incorporating Al – C-A-S-H in cement nomenclature), present results could also be of interest for the modeling of cement material evolution upon alteration by water.

Table 1 | Chemical composition of the hydrotalcite, bentonite, silica fume and CEM III/C components used to produce the cementitious grout

Element	Component			
	Hydrotalcite	Bentonite	Silica fume	CEM III/C
Major elements				
SiO_2 (wt.%)	<Q.L.	47.5	95.3	30.5
Al_2O_3 (wt.%)	18.3	17.0	<Q.L.	10.1
MgO (wt.%)	36.8	3.6	<Q.L.	5.6
CaO (wt.%)	<Q.L.	3.2	0.9	42.2
LOI_{1025} (wt.%)	43.5	18.8	2.2	2.3
Trace elements				
Na_2O (wt.%)	1.7	2.70	<Q.L.	0.60
K_2O (wt.%)	<Q.L.	0.62	0.36	0.38
MnO (wt.%)	<Q.L.	0.04	<Q.L.	0.25
P_2O_5 (wt.%)	<Q.L.	0.12	0.07	<Q.L.
TiO_2 (wt.%)	<Q.L.	0.63	<Q.L.	0.46
Fe				
Total Fe_2O (wt.%)	<Q.L.	4.30	0.16	0.77
Fe(II)/Fe_{tot} (at.%)	<Q.L.	28	<Q.L.	40
Carbon				
C_{tot} (w.%)	2.20	0.79	1.45	0.57
C_{org} (w.%)	<Q.L.	<Q.L.	1.45	<Q.L.
Sulfur				
S(-II) (wt.%)	<Q.L.	0.10	<Q.L.	0.80
S(VI) (wt.%)	<Q. L.	<Q. L.	<Q. L.	2.70
S(0) (wt.%)	<Q.L.	0.09	0.07	0.07

LOI_{1025}, Fe_{tot}, C_{tot}, and C_{org} respectively stand for weight loss upon heating the sample at 1025 °C, total Fe, total C, and organic C. $QL_{SiO2,\ Al2O3,\ MgO,\ Na2O,\ S(VI)}$ = 0.2 wt.%, $QL_{CaO,\ S(-II),\ Ctot,\ Corg}$ = 0.1 wt.%, $QL_{K2O,\ P2O5,\ TiO2,\ S(0)}$ = 0.05 wt.%, QL_{MnO} = 0.02 wt.%, QL_{FeII} = 0.16 wt.%, where QL_{xx} stands for "quantification limit of element XX".

Results and discussion

Characterization of the grout and of its components

Initial anhydrous grout components. The XRD patterns of the silica fume, CEM III/C, bentonite, and hydrotalcite components are shown in Fig. 1, and their chemical composition is provided in Table 1. Information concerning grain size distributions can be found in Supplementary Fig. 1.

Since the hydrotalcite component had no significant content of any anion but had a weight loss at 1025 °C (LOI_{1025} in Table 1) equal to 43.5 wt.%, it could be assumed that hydrotalcite interlayer anion was CO_3^{2-}. Such interpretation was confirmed by calcimetry from which it could be determined that the sample contained 13 wt.% CO_3^{2-}, in close agreement to the theoretical value of 13.3 wt.% that is expected in case of an hydrotalcite containing interlayer CO_3^{2-} ($Mg_4Al_2(OH)_{12}CO_3{\cdot}2H_2O$). The 43.5 wt.% loss at 1025 °C was certainly due to hydrotalcite transformation to MgO and Al_2O_3, as such reaction would in principle induce a 47.7 wt.% loss.

The silica fume and CEM III/C XRD patterns were not refined, because of a high content of amorphous phases. In addition, these two components undergo significant mineralogical transformation during grout hydration, hence limiting the usefulness of the mineralogical quantification, since comparison of phase abundance before and after components mixing and hydration would provide no useful information. From qualitative data examination, the silica fume component mainly contained amorphous silica and minor amounts of quartz and cristobalite. The CEM III/C was also mainly composed of an amorphous component, associated with minor amounts of hatrurite, anhydrite, larnite, calcite, aragonite, C_3A, gypsum,

Table 2 | Cation exchange capacity (CEC) of the bentonite component, and cations and SO_4 extracted after contacting the solid with a cobaltihexamine solution

CEC (meq 100 g^{-1})	Cations (meq 100 g^{-1})						SO_4 (meq 100 g^{-1})
	Na	K	Mg	Ca	NH_4	Σ	
76.0(19)	78.4(11)	1.6(1)	7.7(8)	6.3(18)	0.4(0)	94.2(24)	6.1(1)

Number under brackets are the uncertainty of the last digit (standard deviation, $n = 3$). Σ stands for "sum of cations".

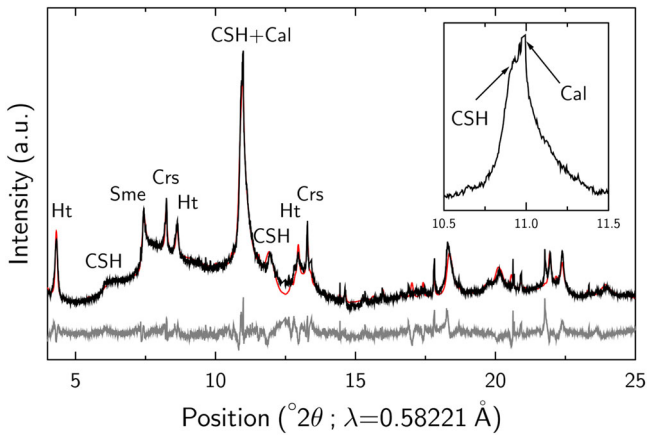

Fig. 2 | Main panel: XRD pattern of the dry sample (black solid), prior to submitting it to the alteration experiment, modeled XRD pattern (red solid line), and difference plot (gray solid line). Main diffraction peaks in the 4–15 °2θ are indexed following Ht hydrotalcite, CSH C-S-H, Sme smectite, Crs Cristobalite, Cal Calcite. The inset (top right) is a magnification of the 10.5–11.5 °2θ region, to highlight the presence of both C-S-H and calcite diffraction maxima.

and brownmillerite. The hydrotalcite component contained 55 wt.% hydrotalcite *sensus stricto* (i.e., having a R-32/m space group[7]), 44 wt.% quintinite (same layer structure as hydrotalcite, but P-62 m space group[8]), and 1 wt.% quartz. Finally, the bentonite component contained 76 wt.% smectite, 8 wt.% albite, 5 wt.% calcite, 3 wt.% sanidine, 3 wt.% quartz, 1 wt.% kaolinite, 1 wt.% talc, 1 wt.% dolomite, and traces (<1 wt.%) of gypsum, magnesite, and anatase.

Using the cobaltihexamine adsorption method, the cation exchange capacity (CEC) of the bentonite component was found to be on average 76 meq 100 g^{-1} (Table 2), in good agreement with literature data (78 meq 100 g^{-1} for the sample "V2" in a previous study[9]). The interlayer was certainly saturated with Na, which was the main cation extracted by cobaltihexamine, with a concentration (78.4 meq 100 g^{-1}) commensurable with the CEC. Minor amounts of Ca were also extracted, with a concentration (6.3 meq 100 g^{-1} on average — Table 2) close to that of SO_4 (6.1 meq 100 g^{-1}). Assuming that Ca and SO_4 originate from gypsum dissolution, the calculated gypsum content would be 0.5 wt.%, thus explaining why it could not be quantified by XRD with the analytical conditions used for this study. The minor amounts of Mg, K, and NH_4 that were extracted certainly result from limited mineral alteration upon contact with the cobaltihexamine solution.

Mineralogy of the sample before its interaction with water. Based on the modeling of its XRD pattern (Fig. 2), the cementitious grout sample used for in situ XRD contained 38 wt.% silica fume, 36 wt.% C-S-H with an occupancy of Si bridging sites of 0.67 (Ca/Si ratio ~0.85), 17 wt.% smectite, 4 wt.% hydrotalcite, 2 wt.% calcite, 3 wt.% cristobalite, and traces of dolomite and feldspars. Total S(-II) content was below the analytical detection limit of 0.1 wt.%. Grain size distribution is provided as an electronic annex (Supplementary Fig. 1). Note that since the cementitious grout was left for curing ~4 years, its mineralogy can be assumed stable over the experimental time of this study. Ettringite was not observed in the present study, while its presence was mentioned in previous works[5,6]. This could be due to a combination of no or low ettringite content in the presently studied cementitious grout, of sample heterogeneity, or of curing time.

Since this refinement was performed on a small quantity of sample due to the small size of the synchrotron beam, the mineralogy may differ from that of the bulk, in particular concerning the proportion of silica fume and smectite. To assess the relevance of the present quantification, the chemical composition that corresponds to the mineralogy of the refined sample was calculated using the molar mass and structural formula of each phase (taken from the Thermoddem database[10]). It was then compared to the bulk chemical composition deduced from the chemistry and mixing proportions of the grout components (Table 1 and materials and methods). Results were in agreement, differing on average by 2 wt.%. Calculations based on XRD refinement and considering only phases having an abundance of 2 wt.% or more led to 63.4 wt.% SiO_2, 17.5 wt.% CaO, 10.6 wt.% Al_2O_3, 7.7 wt.% MgO, and 0.7 wt.% Na_2O. Calculations using the chemical composition of the grout components led to 59.4 wt.% SiO_2, 18.9 wt.% CaO, 6.8 wt.% Al_2O_3, 3.8 wt.% MgO, and 0.6 wt.% Na_2O. Hence, it was considered that the sample exposed to the X-ray beam had a mineralogical composition representative of the bulk sample.

XRD did however not allow determining if the C-S-H phase contained Al in isomorphic substitution to Si, as frequently observed in the literature, because the scattering factors of Al and Si are little different[11]. To investigate this potential incorporation, as well as to gain further insights into sample mineralogy, ^{29}Si and ^{27}Al MAS NMR analyses were conducted. The ^{29}Si MAS spectrum of the cementitious grout and its deconvolution are presented in Fig. 3 and modeling parameters are provided in Table 3.

The resonances at −80.1 ppm and −86.0 ppm correspond to the Q^1 and Q^2 species in C-S-H. It has previously been established that Al can be incorporated in the Si Dreierketten chains (i.e., "silicate chains") of C-S-H by Si substitution for the bridging sites, in a Q^2_B site[12]. The presence of Al in the second coordination sphere of Si produces a high-frequency shift of Q^2 resonances. The signal at −83.4 ppm was hence attributed to Q^2(1Al) and, from now on, C-S-H will be referred to as C-A-S-H. A similar shift is also observed when Al is in a Q^3 site that bridges two tetrahedral chains. The presence of Q^3 units is not unlikely in our case, because the XRD-refined C-A-S-H has a Ca/Si ~0.85 and because C-A-S-H of low Ca/Si frequently have Q^3 sites. Consequently, the signal at -88.2 ppm was attributed to Q^3(1Al), in agreement with previous characterization of Al substituted 11 Å tobermorite[13] and C-A-S-H of low Ca/Si[14,15]. Using the relative abundances of the different ^{29}Si C-A-S-H sites, the mean Si chain length (mean number of Si connected in the Dreierketten chains — MCL) was calculated[16] and found to be 13.6, which translated in a C-A-S-H Ca/Si ratio of 0.79, coherent with the value of 0.85 obtained from XRD. The resonances at −93.5, −102.7 and −109.2 ppm were respectively assigned to Q^3 Si in smectite[17] and Q^3 and Q^4 units of amorphous silica[18]. Finally, the assignment of the two last resonances at −98.5 and −89.4 ppm was ambiguous. They may indicate the presence of hydrated silica. Although its exact nature cannot be elucidated from the sole analysis of ^{29}Si MAS-NMR data, it can be inferred from literature information and mass-balance calculations. Cement hydration leads to the transformation of silica initially present, to form first hydrated silica, then an amorphous phase that is intermediate between silica and C-A-S-H, and finally C-A-S-H. This reaction sequence, which is certainly due to the presence of large particles of densified silica fume (DSF) that are not

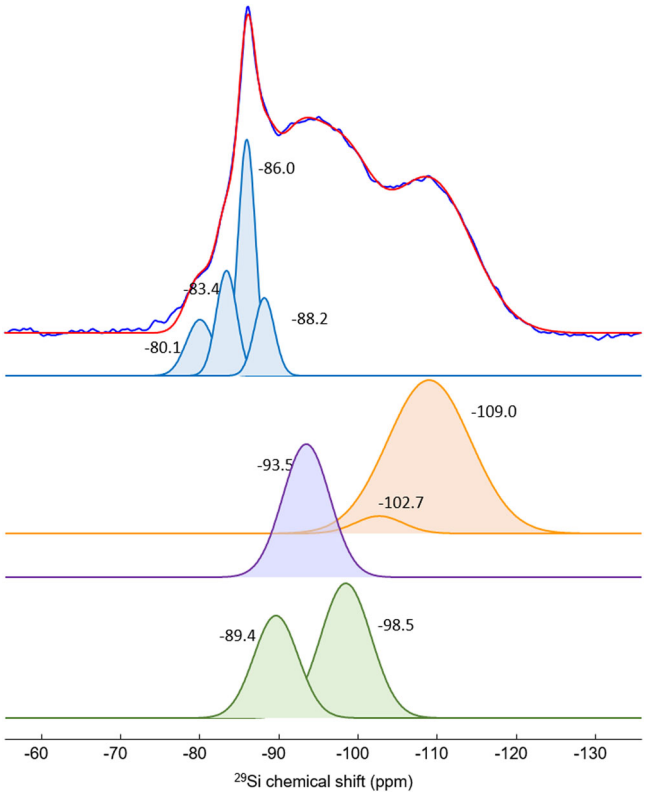

Fig. 3 | ^{29}Si MAS NMR spectrum of the hydrated cementitious grout (blue). The simulated spectra (red) is calculated from the proposed deconvolution (Table 3). Light blue, orange, purple and green lines are respectively attributed to Si in C-A-S-H, silica fume, smectite, and hydrated silica phases.

Table 3 | NMR parameters and assignment of the different components of the ^{29}Si MAS-NMR signal

Component	Proportion (%)	Chemical shift (ppm)	Width (ppm)	Assignment
1	3.8	−80.1	4.1	Q^1 C-S-H
2	5.3	−83.4	3.0	Q^2(1Al) C-A-S-H
3	10.0	−86.0	2.6	Q^2 C-S-H
4	3.9	−88.2	3.0	Q^3(1Al) C-S-H
5	15.5	−93.5	7.0	Smectite
6	31.5	−109.0	12.4	Q^4 Silica
7	2.0	−102.7	7.1	Q^3 Silica
8	16.8	−98.5	7.5	Hydrated silica
9	11.2	−89.4	6.6	Hydrated silica

All components fitted with a Gaussian-like shape[38].

fractioned during the synthesis process of the grout[5], was frequently observed here using EPMA and manifested itself by the presence of grains having a SiO_2 core while, when going from this core to the outside, a progressive incorporation of Ca was observed (Fig. 4).

It is proposed here to attribute the resonance at −89.7 ppm to the reacted silica and (or) to the amorphous intermediate phase. This is supported by mass-balance calculations: with the resonance at −89.7 ppm attributed to silica, the proportions of the different ^{29}Si MAS-NMR sites, and using C-A-S-H, smectite, and SiO_2 molar masses, the relative proportions of C-A-S-H/smectite/SiO_2 could be calculated to be 41/17/42, in good agreement with quantification based on XRD data (39/19/42).

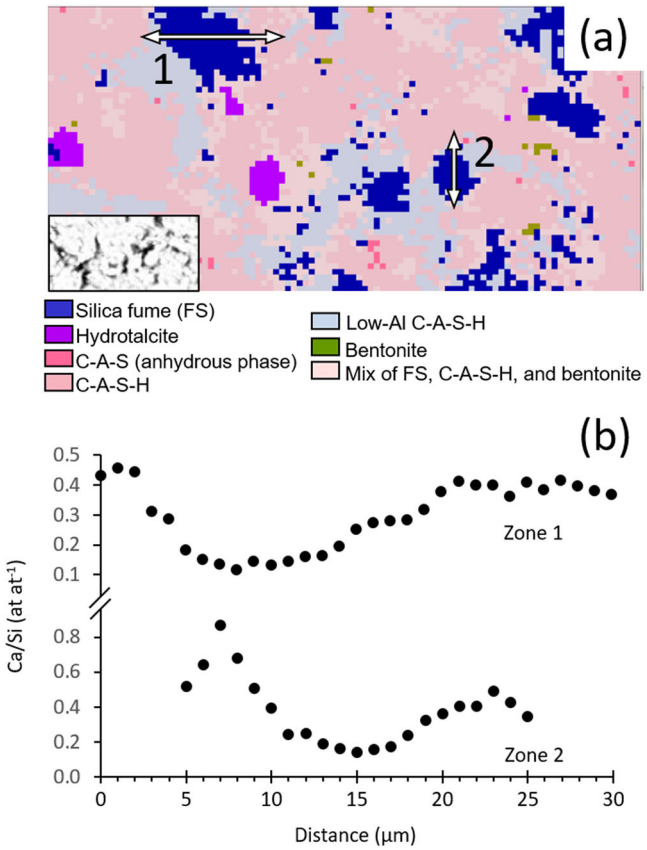

Fig. 4 | EPMA analysis of a hydrated cementitious grout. a Mineralogical mapping obtained from the EPMA analysis of a pristine hydrated cementitious grout. Identification performed based on a ternary diagram provided in Supplementary Fig. 2. Pixel size is 1 × 1 μm. The two white arrows point out to two profiles along reacted silica fume. The inset at the bottom is the back-scattered electron map of the same area. Ca/Si atomic ratios over these profiles are shown in (**b**).

Further investigation of sample mineralogy was done using ^{27}Al MAS NMR. The spectra obtained for the cementitious grout and the three anhydrous grout components containing Al (Table 1) are presented in Fig. 5.

The ^{27}Al MAS NMR signal of the hydrated cementitious grout had three main components, two located between 0 and 15 ppm and attributed to aluminum in octahedral coordination (Al_{VI}) and one dissymmetric broad signal centered at around 60 ppm and corresponding to aluminum in tetrahedral coordination (Al_{IV}). The deconvolution of the spectrum from the cementitious grout is presented in Fig. 6, and associated NMR parameters are provided in Table 4. Deconvolution was done by performing complementary 2D MQ-MAS experiment (Supplementary Fig. 3 and Supplementary Table 4). The sharp Al_{VI} signal at δ_{iso} = 10.2 ppm may correspond in principle to several hydrated phases (e.g. AFm or hydrotalcite). However, the similarity with the signal found in the spectrum of the hydrotalcite used to produce the sample (Fig. 5) and the fact that XRD did not detect phases such as AFm (see above) allowed assigning the resonance at 10.2 ppm to Al_{VI} incorporated in hydrotalcite. The similarity with the peak observed for pure hydrotalcite indicated the absence of significant structure modification during the grout hydration process. The wide resonance at δ_{iso} = 7.4 ppm was attributed to smectite Al_{VI}, with this mineral originating from the bentonite component. The smectite Al_{IV} observed in the bentonite spectrum was too weak to be observed in the spectrum of the hydrated cementitious grout. Two Al_{IV} resonances were observed at δ_{iso} = 59.2 ppm and δ_{iso} = 67.1 ppm. These resonances were observed previously in Al-substituted tobermorite[19] and C-A-S-H with Ca/Si ratios of 0.75 and 0.83[19]. Sun et al.[15] reported that, when sample Ca/Si is 1.25 or more, these resonances are associated to additional ones at ~75 ppm and attributable to Al_V

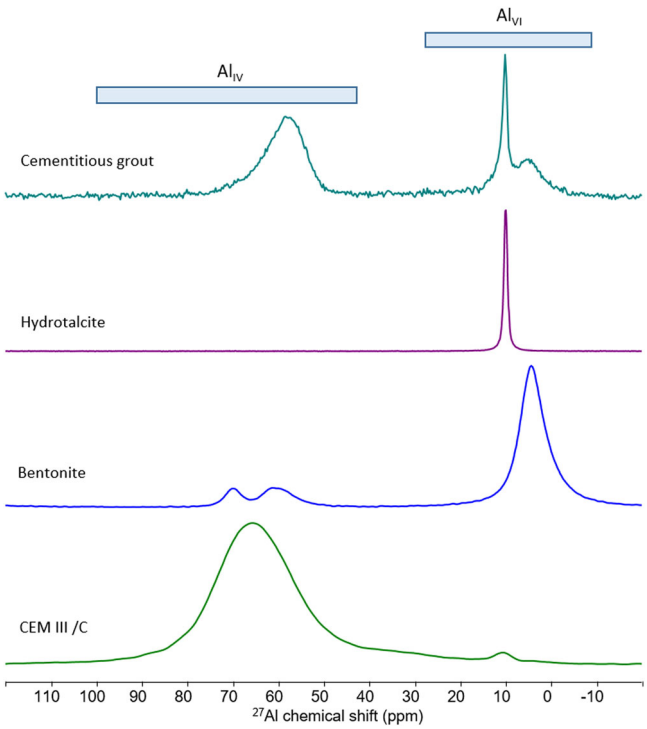

Fig. 5 | ^{27}Al MAS-NMR signals of, from top to bottom, the hydrated cementitious grout, and the hydrotalcite, bentonite, and CEM III/C components. The chemical shifts intervals in which tetrahedral Al (Al_{IV}) or octahedral Al (Al_{VI}) resonances can be observed are approximate.

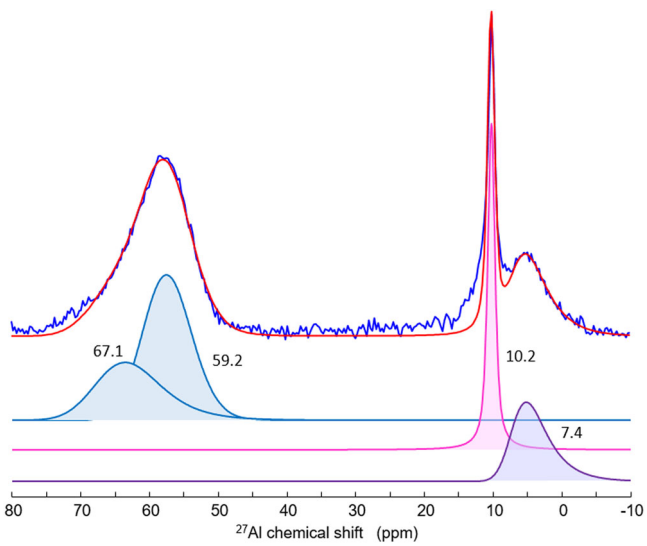

Fig. 6 | ^{27}Al MAS NMR spectrum of the hydrated cementitious grout (blue). The simulated spectra (red) is calculated from the proposed deconvolution. Light blue, pink and purple lines are respectively attributed of aluminum in C-A-S-H, hydrotalcite and bentonite phases.

and Al_{VI}. The absence of such additional resonances in the present data further supports the conclusion that the C-A-S-H in the hydrated cementitious grout has a low Ca/Si. However, it must be noted that the nature of these additional resonances is unclear, as C-A-S-H Ca/(Si + Al) atomic ratio cannot exceed values significantly higher than ~1.3. Above this value, the increase in bulk Ca/Si is due to the presence of additional discrete phases, such as nanocrystalline portlandite[16,20,21]. Finally, in the presently studied sample, there was no signal attributable to a slag remnant.

Table 4 | NMR parameters and assignment of the different components of the ^{27}Al MAS NMR spectrum

Component	Proportion (%)	δ_{iso} (ppm)	C_Q (MHz)	Width (ppm)	Assignment
1	22.8	67.1	5.8	–	Al_{IV} C-A-S-H
2	41.2	59.2	3.6	–	Al_{IV} C-A-S-H
3	18.4	10.2		1.3	Al_{VI} hydrotalcite
4	17.6	7.4	4.9	-	Al_{VI} Smectite

Hydrotalcite resonance was fitted with a Gaussian-Lorentzian-like shape whereas the three other lines were simulated using the Czsimple model implemented in the Dmfit software[38], adapted to the case of disordered phases.

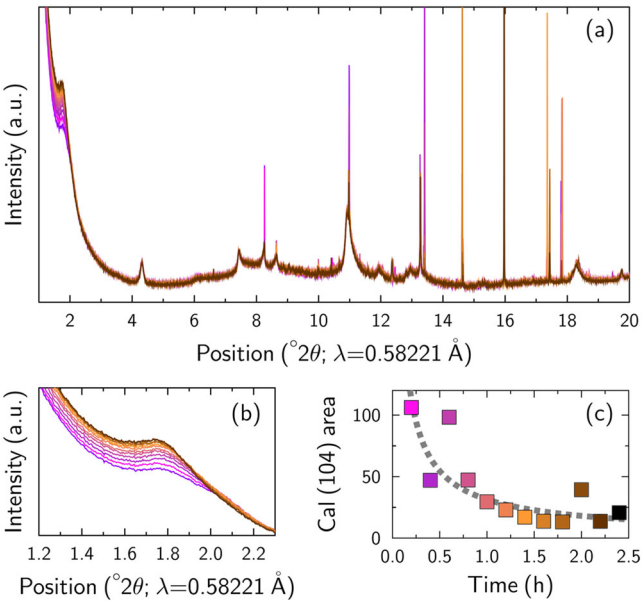

Fig. 7 | Time-resolved XRD of the cementitious grout upon alteration by water. **a** Time-resolved XRD of sample evolution when contacted with double distilled water. Time increases in the order pink to orange to black. One pattern was collected every 12 min. **b** Detailed view of the 1.2–2.3 °2θ region. **c** evolution of the area of the calcite (104) reflection as a function of time. The dotted gray line is a guide to the eye.

Mineralogical evolution during percolation by water

When the cementitious grout was flowed with double distilled water, the change in XRD signal as a function of time and hence the evolution of the solid phase was limited (Fig. 7). The two significant modifications that could be observed were the appearance and increase in intensity of a diffraction maximum at ~1.75° 2θ (~19 Å, Fig. 7b) attributable to smectite and the weakening of calcite diffraction maxima, down to negligible intensity after 1.5 h of experiment (Fig. 7c). These two evolutions are diagnostic for, respectively, progressive saturation of smectite interlayer with Ca^{2+} hydrated by three H_2O planes in the interlayer, and dissolution of calcite. Since smectite interlayer was initially saturated with Na^+ (Table 2), both phenomena were possibly coupled, with calcite dissolution being a source of aqueous Ca^{2+}, which was then adsorbed in smectite interlayer through a Ca/Na exchange mechanism. In addition, the main C-A-S-H diffraction maxima seemed to weaken slightly. This would be indicative of slight dissolution, but the evolution remained within uncertainties.

XRD data were transformed to PDF (Fig. 8a) to gain better insights into the chemical evolution of the system as a function of time. Such transformation could not be done for the two data collected after 1.2 and 1.4 h of contact time because of too intense preferential orientation effects. In the PDF data, the correlations at ~1.6 Å and ~2.4 Å, assumed attributable to Si-O and Ca-O correlations, were used to estimate the evolution of the Ca/Si

molar ratio of the whole sample as a function of contact time. This Ca/Si ratio was found to be constant during the experiment with a mean value of 0.10(3) mol mol^{-1} (Fig. 8b). This value was commensurable with the value of 0.19 mol mol^{-1} that can be recalculated using the quantitative mineralogical composition determined from the modeling of the XRD patterns, including C-A-S-H refined Ca/Si atomic ratio (see above), and using molecular masses and structural formula from the Thermoddem database[10]. The slightly lower Ca/Si value certainly results from an uncertainly in the estimation of the amorphous silica content by XRD and (or) from sample heterogeneity. Yet, this allowed concluding that no significant evolution of bulk Ca/Si, and hence certainly C-A-S-H Ca/Si, occurred during the experiment. Hence, if limited C-A-S-H dissolution occurred, it was certainly congruent, consistent with our currently knowledge of the mechanisms of C-A-S-H alteration, with congruency being only observed for Ca/Si ratio close to 0.83 (i.e. close to the presently studied C-A-S-H), while a preferential release of Ca is observed for C-(A-)S-H of higher Ca/Si ratio[22,23].

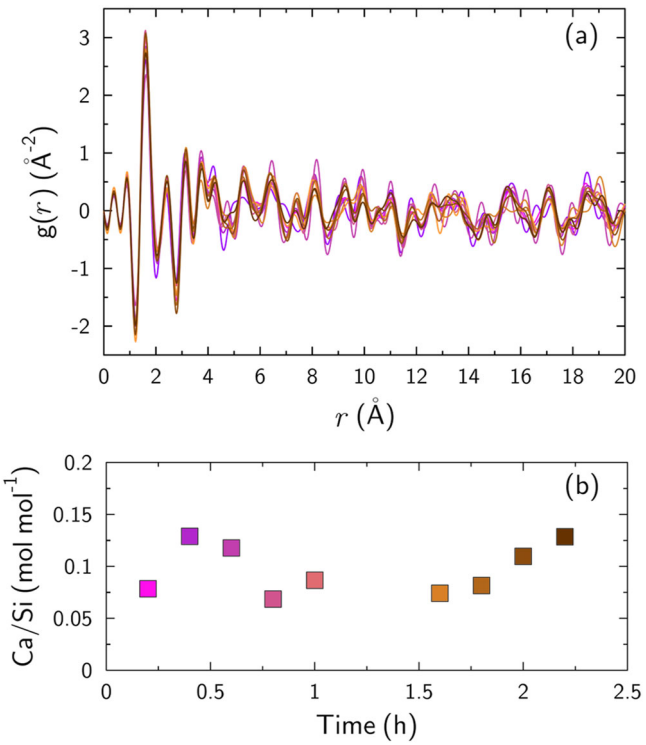

Fig. 8 | Time-resolved X-ray PDF of the cementitious grout upon alteration by water. Time-resolved (**a**) PDF of sample evolution when contacted with double distilled water and (**b**) Ca/Si ratio calculated from areas of Ca-O and Si-O peak areas (see text for details). Same color coding as in Fig. 7.

To conclude, from a mineralogical point of view, the transformations that were observed upon leaching with double distilled water was calcite dissolution, a change in smectite interlayer composition, from Na-saturated to Ca-saturated, and possibly a slight and congruent dissolution of C-A-S-H.

A mechanistic and thermokinetic model for grout degradation

The mineralogical characterization performed above evidenced that the cementitious grout has a complex mineralogy made of crystalline, cryptocrystalline, and amorphous phases, with a however relatively limited mineralogical evolution during alteration with double distilled water (see previous section). To build a thermokinetic model, not only the mineralogical evolution, but also the changes in solution chemistry as a function of sample alteration must be quantified and modeled satisfyingly. For this purpose, flow-through experiments were carried out by contacting the cementitious grout with double distilled water equilibrated with given CO_2 partial pressures. These experiments had two purposes: first, evaluate the kinetics of reactivity of the different phases building up the cementitious grout and, second, build a quantitative and predictive model taking into account phase evolution (dissolution, precipitation, recrystallization). The optimized mineralogical assemblage, which allowed the best reproduction of solution chemistry data, is presented in Table 5. The relative amounts of C-A-S-H, silica fume, and smectite were 32/53/15 and compared well with XRD (39/42/19), ^{27}Si NMR (41/42/17), and amounts deduced from the proportion of each anhydrous component (47/44/9), hence demonstrating the coherency of the different characterization techniques. Minor differences must however be noted, especially with regards with minor phases. In particular, the presence of a sulfate-bearing phase (gypsum was selected here based on trace amounts detected by XRD in the initial products and on indirect evidence from the CEC experiment, see above) was mandatory to model satisfyingly aqueous data. The fact that it was not detected during mineralogical analyses is probably related to its low abundance (see discussion relative to gypsum above) and (or) to sample heterogeneity.

To model pH and Ca and Si concentration, the initial Ca/Si ratio of C-S-H had to be set to 0.86 using a modified version of the SiO_2/C-S-H/$Ca(OH)_2$ model of Walker et al.[24], in agreement with XRD and NMR data (see above). The evolution of pH, alkalinity and Ca concentration were simulated satisfyingly whereas the experimental and modeled Si concentration had minor discrepancy, mainly at early stages of alteration (Fig. 9). The minor difference between experimental and calculated Si evolution, in particular at the early stages of alteration, may be attributed to heterogeneities regarding the grout composition, the reactive surface area of Si-bearing phases, and (or) the exact nature of the amorphous silica. For example, silica fume and hydrated silica fume certainly have different solubility, but the absence of thermodynamic and kinetics data relative to hydrated silica precluded inclusion of this potential effect in the model. As expected from previous studies that showed that C-S-H dissolution is congruent when structural Ca/Si ratio is close to 0.8[22–24], and coherent with the PDF analysis above, the modeled Ca/Si ratio of the C-S-H remained

Table 5 | Mineralogical assemblage considered for the modeling of flow-through experiments

Name in THERMOCHIMIE	Amount (mol l^{-1})	Kinetics	Remarks
CSH0.8[a]	8.0 10^{-3}	Yes	End-member of an ideal solid solution (modified from Walker et al.[24])
Portlandite[b]	5.0 10^{-4}	Yes	End-member of an ideal solid solution (modified from Walker et al.[24])
Hydrotalcite-CO_3	2.1 10^{-4}	Yes	Anionic exchange no taken in account (see main text for details)
Calcite	1.5 10^{-3}	Yes	
SiO_2(am)	3.0 10^{-2}	Yes	
Montmorillonite-BCNa	1.2 10^{-3}	Yes	Cationic exchange from (Tournassat et al.[43])
Gypsum	8.0 10^{-4}	No	
Gibbsite	2.0 10^{-4}	No	

[a]Actual Ca/Si ratio modified by introducing "portlandite".
[b]Does not occur as a discrete phase. Used to set the C-S-H Ca/Si ratio.

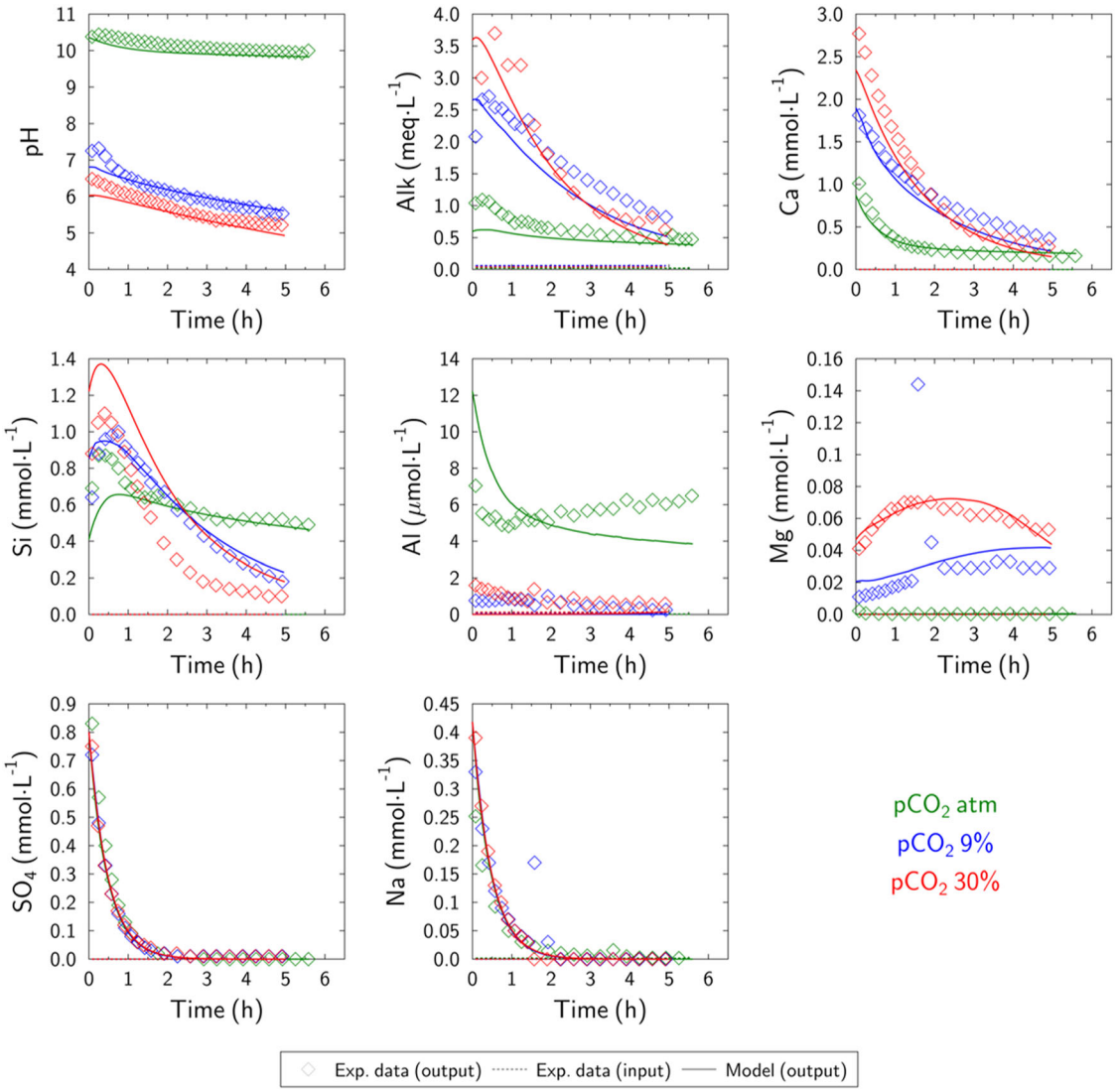

Fig. 9 | Effect of the CO_2 partial pressure on the alteration of the cementitious grout interacting with double distilled water at ~25 °C. Green, blue and red lines and symbols refers to experiments conducted by using double distilled water equilibrated with atmospheric partial pressure, with a 9% CO_2/91% N_2 gas mixture, and with a 30% CO_2/70% N_2 mixture.

almost constant during the experiments (~0.8). The SO_4 evolution stemmed from the instantaneous dissolution of gypsum ($CaSO_4$:$2H_2O$) during the flooding of the reactor, while the Na evolution was due to Na/Ca exchange in smectite interlayer. The change in smectite interlayer composition from Na-saturated to Ca-saturated was promoted by both gypsum and (or) calcite dissolution, the latter mechanism being observed by in situ XRD experiments (see above). Except for the cationic composition of the exchanger, the smectite was stable along the experiment in both experiments and models. Hydrotalcite is in principle an anionic exchanger[25]. However, the affinity for carbonate anions is high and sorption appears to be hardly reversible once the interlayer is saturated with CO_3^{2-}[26]. In agreement, the anion exchange reactions were tested but finally discarded in the models because, in the best case, they did not allow improving the quality of data modeling. Al and Mg were released due to hydrotalcite dissolution. Note that hydrotalcite alteration could possibly be accompanied by the formation of a gibbsite passivation layer at pH > 4. Such a secondary phase formation, which would be hardly detectable by in situ XRD due to low amounts precipitated and to potential amorphous or nanocrystalline nature of the Al-rich phase, would drastically decrease the dissolution rate of hydrotalcite[27,28]. In this study, a congruent dissolution was considered and was sufficient to reproduce well enough Al and Mg variations during the experiments. Hydrotalcite dissolution was visible by XRD once submitted to a water that contained 30 vol.% of CO_2 (40 wt.% lost—Fig. 10), otherwise it remained close to the initial concentration within uncertainties. In any case, experiments and models agreed on the remaining quantities at the end of the experiment (Fig. 10). One of the most significant changes from a mineralogical point of view was the decrease of the C-A-S-H content that initially represented one third of the material and decreased down to ~5 % once submitted to a water highly enriched in CO_2 (30 vol.%). Sample dissolution was related to the experimental conditions: the more the CO_2 in solution, the more the dissolution. Indeed, upon lixiviation 22 wt.% of the material were lost in atmospheric condition, 31 wt.% with a partial pressure of CO_2 of 9 vol.% and 34% with a partial pressure of CO_2 of 30 vol.%. The water used was highly corrosive toward C-A-S-H and calcite, and therefore, the mass loss was mostly due to the decreased abundance of those two phases. Finally, the quantities of each mineral at the end of the modeling compared well with XRD analyses (Fig. 10) and the cement degradation sequence (including C-A-S-H carbonation) was well captured by the model.

Concluding remarks

The aim of this study was twofold: First, determining the mineralogical and geochemical composition of a cementitious grout designed to

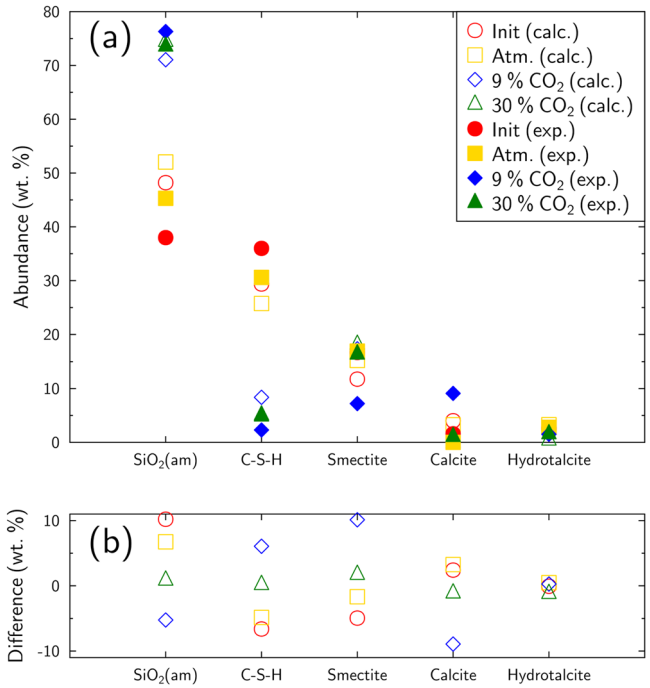

Fig. 10 | Comparison of the relative mineral abundances determined from XRD and thermokinetic modeling. a Relative abundance of minerals initially present in the cementitious grout and after experiments. Circles, squares, diamonds and triangles respectively refer to the initial mineralogical composition, and to experiments conducted at atmospheric CO_2 conditions, 9% CO_2, and 30% CO_2. Open symbols: quantities estimated from thermokinetic modeling. Full symbols: quantities estimated from mineralogical (XRD—Supplementary Fig. 4) characterization. **b** Difference between quantities estimated from the mineralogical analysis and from the thermokinetic modeling. Symbols as in top panel.

buffer perturbations induced by excavation and subsequent claystone desaturation and oxidation in the fractured zone that occurs in the close vicinity of the drilling area. Second, building a thermokinetic model for this cementitious grout[5]. It could be observed that upon leaching with double distilled water, pH always remained lower than 10.5, with increasing alteration time and increasing CO_2 partial pressure both decreasing pH.

The thermokinetic model developed here, grounded on a sound mineralogical description of the solid phase, allowed reproducing satisfyingly the evolution of the cementitious grout on short time scale. In addition to thermodynamic equilibrium, this model also quantitatively described the kinetics dissolution of the primary minerals composing the cementitious grout. The model is useable for modeling of long-term experiments with more complex geometries. However, as the concept of high-level waste disposal relies on multi-material barriers, the modeler has to keep in mind that to accurately describe the interactions between those materials it is necessary to understand the alteration of each material, their crossed interactions and in particular, the nature and abundance of secondary phases formed due to these interactions. Therefore, specific experiments involving all the materials of the multi-barrier design where diffusion is the driving force of the transport of aqueous species have to be carried out and modeled to be able to extrapolate this model beyond the time and space scales of the laboratory (e.g. to the scale of a waste canister or a disposal site). In addition, it must be reminded that the experiments were conducted here with double distilled water, which is strongly aggressive, in order to obtain kinetics laws of dissolution. In actual geological storage conditions, its leaching behavior will certainly be impacted by numerous parameters including sample microstructure, pore water composition, or temperature, for example. These aspects should be investigated as well in future works.

Methods

Synthesis of the cementitious grout

The first step in producing the cementitious grout consisted in mixing 8 kg m^{-3} hydrotalcite, 33 kg m^{-3} "Milos" bentonite[9], 126 kg m^{-3} silica fume and 126 kg m^{-3} CEM III/C, all of commercial grade quality, stored as received, and characterized in the following. The mixing procedure is described in details by Bonnet et al.[5]. The volumic solid:liquid ratio was equal to 30:70. The same grounded and sieved (cut-off diameter of 80 µm) sample was used for all experiments and characterizations.

Chemical analyses

Total chemical compositions of the solids were determined, following a triacid attack (HCl, HNO_3, HF) on bulk powder, using inductively coupled plasma atomic emission spectroscopy (ICP-AES, Jobin Yvon) or mass spectroscopy (ICP-MS, Thermo Fisher Scientific) depending on the element concentration for trace elements. For the major elements (Al, Ca, Fe, K, Mg, Mn, Na, P, Ti, and Si, expressed as Al_2O_3, CaO, Fe_2O_3, K_2O, MgO, MnO, Na_2O, P_2O_5, TiO_2 and SiO_2, respectively) the concentrations were double-checked by X-Ray fluorescence (XRF, Zétium from Panalytical).

Total S was determined in accordance with NF ISO 15178 by dry combustion. S(-II) was determined after leaching of the S(VI) species soluble in Na_2CO_3 and quantification of the remaining sulfur in the solid using dry combustion. S(VI) was quantified by precipitation of the S(VI) species soluble in Na_2CO_3 as barium sulfate and gravimetric measurement. S(0) was deduced from the difference between total S and the sum of S(-II) and S(VI).

Fe speciation was assayed in the solids through a modified 1,10-phenanthroline method[29].

Calcite and dolomite were quantified using a Bernard calcimeter. Briefly, the sample was placed in a test tube and then contacted with HCl. The CO_2 formed during the reaction displaced water present in a graduated cylinder from which the quantity of carbonate originally present in the sample was read.

Total organic carbon was quantified using a Jobin Yvon EMIE 820 V carbon analyzer after acidic treatment of the sample to remove carbonates.

Solution pH was measured with a Metrohm pH-meter after calibration with NIST pH 4, 7, and 10 buffers. Inductively coupled plasma atomic emission spectroscopy (ICP-AES, Jobin Yvon) or mass spectroscopy (ICP-MS, Thermo Fisher Scientific) was used to measure aqueous Ca, K, Mg, Na, Sr, Fe, Al and Si concentrations. Cl and SO_4, were analyzed by ionic chromatography (HPLC, Dionex). The concentrations of elements in solution were determined with a relative uncertainty of 3%.

Alkalinity was measured using a Titrando 905 and a Dosino 800 equipped with a 5 ml syringe (Metrohm) to gradually inject an HCl solution (10^{-3} mol l^{-1}) into the sample. The alkalinity was calculated with the Gran method[30].

Electron microprobe microanalyses

X-ray intensity maps of major elements (Si, Al, Fe, K, Na, Ca, Mg, and S) were acquired using a Cameca SX Five electron microprobe with an accelerating voltage of 15 kV and a current beam of 30 nA. Na Kα and Mg Kα peak intensities were monitored on LTAP (Large Thallium Acid Phthalate) monochromator crystal, Si Kα and Al Kα peak intensities on TAP crystal, K Kα peak intensity on PET (Pentaerythritol) crystal, Ca Kα and S Kα peak intensities on LPET (Large Pentaerythritol) crystal, and Fe Kα peak intensity on LIF (Lithium Fluoride) crystal. The dwell time was 100 ms per pixel. The background was measured independently and subtracted from X-ray emission peaks. After the acquisition, no evidence of beam damage was identified on the mapped area.

In situ synchrotron X-ray diffraction

In situ synchrotron X-ray diffraction (XRD) experiments were performed at beamline CRISTAL from the SOLEIL synchrotron, using an energy of 21.3 keV (λ = 0.58221 Å). The experimental set-up used in this study is described in details in previous works concerning the reactivity Mn and Fe (oxy)hydroxides, layered double hydroxides, and cement phases[22,31–33].

Briefly, a polyimide capillary (internal diameter: 1.47 mm, wall size: 0.05 mm) was filled with, successively, 20 mg of glass beads and 20 mg of the cementitious grout that was previously crushed and sieved to a cut-off diameter of 80 µm. It was then sealed on both sides by a frit, connected on one side to a peristaltic pump and on the other side to an empty recipient. It was exposed to the X-ray beam and flowed with double distilled water. The glass beads, located on the side opposite to the peristaltic pump, prevented the cementitious grout from migrating to the frit. In a first step and before flowing the sample with the solution, several XRD patterns were collected along the dry capillary with a twofold aim: First, determining the most suitable area for data collection (defined as an area where all phases from the sample were present and where sample density was high, to improve signal-to-noise ratio). Second, collecting a pattern that was used for quantitative analysis of the mineralogical assemblage. The obtained dried pattern was modeled with the Profex graphical interface to the BGMN software[34], after removal of the signal from abnormally intense peaks resulting from preferential orientation. All phases used for refinement were those of the BGMN database, except for two cement phases. The first one was C-S-H, whose structure model was that proposed by Grangeon et al.[35], i.e. a defective, nanocrystalline, and turbostratic tobermorite in which the occupancy of bridging Si tetrahedra in the dreierketten (silica) chains was refined. The second was hydrotalcite. It was observed (see below) that this component of the cementitious grout was composed of hydrotalcite *sensus stricto* and of quentinite (having the same layer structure as hydrotalcite but different layer stacking). However, introducing both hydrotalcite *sensus stricto* and quentinite in the modeling led to numerical convergence issue, probably due to a lack of information (undistinguishable *hkl* reflection, with h and/or $k \neq 0$) in the XRD pattern. Rather, two hydrotalcite (*sensus stricto*) structures, differing only by their layer-to-layer distance (7.6 Å and 7.8 Å), were used for modeling the XRD pattern.

In a second step, the solution was flowed through the capillary, and 2D XRD patterns were collected continuously over the 0–120 °2θ interval (equivalent to q values ranging from ~0 to 18.7 Å^{-1}), with a collection time of 12 min per pattern. XRD data were processed using an in-house developed software[36], and converted to X-ray pair distribution function data (PDF) using the software pdfgetx3[37]. For conversion to PDF, background was removed by subtracting from the data the pattern of an empty capillary filled with double distilled water, and the q interval was 0.2 to 14 Å^{-1}.

Sample Ca/Si atomic ratio was calculated from the PDF data, using the ratio of the areas of the correlations at ~2.4 Å and ~1.6 Å, assumed to be respectively attributable to Ca-O and Si-O atomic pairs. The equation used to transform the ratio of areas to atomic ratios was derived from the analysis of the PDF data from Grangeon et al.[21], who studied various C-S-H samples having bulk Ca/Si ratios ranging between 0.57 and 1.47.

^{27}Al and ^{29}Si MAS-NMR

The ^{29}Si MAS NMR spectra of about 200 mg of the lyophilized sample were obtained on a Bruker AVANCE II 400 MHz (B0 = 9.4 T) operating at 79.4 MHz and using a spinning speed of 10 kHz. ^{29}Si chemical shifts are given relative to signal of tetramethylsilane (TMS). Around 6500 scans were added using a π/4 pulse and a recycle delay of 30 s, ensuring complete signal relaxation. The ^{27}Al high-resolution NMR spectra were obtained on a Bruker AVANCE III 850 instrument (principal field 20T–850 MHz) operating at 221.6 MHz, equipped with high-speed MAS probe head (spinning rate of 30 kHz in Al-free zirconia rotors with diameter 2.5 mm). The 1D MAS spectra were acquired after a single short pulse (π/18) ensuring quantitative excitation and quantification of ^{27}Al central transition. Around 11000 scans were accumulated with a recycling delay of 1 s. ^{27}Al chemical shifts were referenced relative to the signal of $Al(NO_3)_3$ 1 M solution. All the spectra were deconvoluted using the Dmfit program[38].

Flow-through experiments

The chemical evolution of the cementitious grout upon alteration by double distilled water was studied using a flow-through reactor previously used to study the alteration of pure mineral phases (clays[39], layered double hydroxides[33], C-S-H[22]) and rocks[40]. Briefly, ~0.4 g of cementitious grout that was previously dried, crushed, sieved to a cut-off diameter of 80 µm, and stored in a glove box under N_2 atmosphere, was introduced in a reactor having a volume of 84 ml. Double distilled water was flowed in this reactor at a rate of ~180 ml h^{-1}. pH and temperature were continuously monitored at the output of the reactor. The output solution was collected and sampled every 10 min. It was then separated in three aliquots: two aliquots were used as sampled for anion quantification and for alkalinity quantification, and the last aliquot was acidified to pH < 3 with ultrapure HNO_3 for cation quantification. To better constrain the kinetics of cement phases dissolution, three different experiments were conducted using double distilled water equilibrated with different gas phases: atmospheric partial pressure, a 9% CO_2/91% N_2 gas mixture, or a 30% CO_2/70% N_2 mixture. Those chosen CO_2 contents stemed from the measured CO_2 content on site during an oxidation experiment (~10 vol%[2]). The maximum value used in this study is higher than the highest value measured on site to maximize cementitious grout reactivity toward carbonation processes. Experiments were modeled using PHREEQC3[41] and THERMOCHIMIE v10 database[42] following the strategy described in a previous study[33]. Briefly, all relevant physical and chemical parameters were continuously monitored, including temperature and flow rates, and accounted for in the modeling. For example, temperature was used to accurately calculate parameters such as activity coefficients. The mineralogical composition considered for the modeling was guided by results from X-ray diffraction. When needed, phase abundance was adjusted to match measured solution chemistry. It was ensured that difference between phase abundance considered during the modeling and results from X-ray diffraction were consistent within 10 wt.% (see "Results and discussion"). Additional phases as compared to X-ray diffraction were introduced at trace concentration when needed, i.e. to reproduce the concentration of elements that could not be explained by using only the mineralogical assemblage determined by X-ray diffraction. Gypsum was added to model the sulfate release at the early stage of the flow-through experiment. Ettringite could have equally been used but was discarded based on ^{27}Al NMR data that did not allow detecting this phase (see "Results and discussion") and because the NMR detection limit is equal to a few hundreds of ppm. Amorphous silica contributed in the modeling of Si concentration. Note that several types of amorphous silica were observed by ^{29}Si NMR (see "Results and discussion") but could not be accounted for during the modeling due to a lack of thermodynamic and kinetic data. The most reactive phases (namely gypsum and gibbsite) were considered at thermodynamic equilibrium, whereas dissolution kinetics were taken into account for all other phases. Kinetics were adjusted to quantitatively reproduce the output concentration of the chemical elements present in the corresponding phase. When dissolution constants were available from literature studies, reactive surface areas were adjusted, and when no data was available from the literature, an overall dissolution rate (dependent on both surface area and dissolution constant) was determined. A single model was used for all the experiments, with the sole difference being the CO_2 partial pressure of the inlet solutions. Experimental data are available as Supplementary Data (Supplementary Tables 1–3).

Data availability

Chemical data from the flow-through experiments are available in the Supplementary Data. Other data available from the corresponding authors on reasonable request.

Received: 18 January 2024; Accepted: 28 June 2024;
Published online: 17 July 2024

References

1. Diler, E. et al. Potential influence of microorganisms on the corrosion of the carbon steel in the French high-level long-lived nuclear waste disposal context at 50°C. *Mater. Corros.* **74**, 1777–1794 (2023).
2. Vinsot, A., Leveau, F., Bouchet, A. & Arnould, A. Oxidation front and oxygen transfer in the fractured zone surrounding the Meuse/Haute-Marne URL drifts in the Callovian–Oxfordian argillaceous rock. *Geol. Soc. Spec. Publ.* **400**, 207–220 (2014).

3. Vinsot, A., Lundy, M. & Linard, Y. O2 consumption and CO2 production at Callovian-Oxfordian rock surfaces. *Procedia Earth Planet. Sci.* **17**, 562–565 (2017).
4. Michau, N. & Bourbon, X. Coulis cimentaire pour remplissage d'un espace annulaire autour d'une alvéole de stockage de déchets radioactifs creusée dans un milieu argileux. France Patent (2014).
5. Bonnet, J. et al. Chemical and mineralogical characterizations of a low-pH cementitious material designed for the disposal cell of the high-level radioactive waste (HLW). *Cem. Concr. Res* **162**, 107013 (2022).
6. Goethals, J. et al. Interaction between carbon steel and low-pH bentonitic cement grout in anoxic, high temperature (80 °C) and spatially heterogeneous conditions. *Corros. Sci.* **211**, 110852 (2023).
7. Bookin, A., Cherkashin, V. & Drits, V. Polytype diversity of the hydrotalcite-like minerals II. Determination of the polytypes of experimentally studied varieties. *Clay Clay Min.* **41**, 558–564 (1993).
8. Arakcheeva, A., Pushcharovskii, D. Y., Rastsvetaeva, R., Atencio, D. & Lubman, G. Crystal structure and comparative crystal chemistry of $Al_2Mg_4(OH)_{12}(CO_3)\cdot 3H_2O$, a new mineral from the hydrotalcite-manasseite group. *Crystallogr. Rep.* **41**, 972–981 (1996).
9. Ohrdorf, K. H., Kaufhold, S., Rüßmann, F., Ufer, K. & Flachberger, H. The unusual behavior of a Milos bentonite in cement suspensions. *Appl. Clay Sci.* **54**, 189–195 (2011).
10. Blanc, P. et al. Thermoddem: a geochemical database focused on low temperature water/rock interactions and waste materials. *Appl. Geochem.* **27**, 2107–2116 (2012).
11. Waasmaier, D. & Kirfel, A. New analytical scattering-factor functions for free atoms and ions. *Acta Crystallogr. Sect. A* **51**, 416–431 (1995).
12. Richardson, I. G., Brough, A. R., Brydson, R., Groves, G. W. & Dobson, C. M. Location of aluminum in substituted calcium silicate hydrate (C-S-H) gels as determined by 29Si and 27Al NMR and EELS. *J. Am. Ceram. Soc.* **76**, 2285–2288 (1993).
13. Maeshima, T., Noma, H., Sakiyama, M. & Mitsuda, T. Natural 1.1 and 1.4 nm tobermorites from Fuka, Okayama, Japan: chemical analysis, cell dimensions, 29Si NMR and thermal behavior. *Cem. Concr. Res.* **33**, 1515–1523 (2003).
14. Richardson, I. G., Skibsted, J., Black, L. & Kirkpatrick, R. J. Characterisation of cement hydrate phases by TEM, NMR and Raman spectroscopy. *Adv. Cem. Res.* **22**, 233–248 (2010).
15. Sun, G. K., Young, J. F. & Kirkpatrick, R. J. The role of Al in C–S–H: NMR, XRD, and compositional results for precipitated samples. *Cem. Concr. Res.* **36**, 18–29 (2006).
16. Richardson, I. Model structures for C-(A)-S-H(I). *Acta Crystallogr. Sect. B* **70**, 903–923 (2014).
17. Fernández, R., Ruiz, A. I. & Cuevas, J. Formation of C-A-S-H phases from the interaction between concrete or cement and bentonite. *Clay Min.* **51**, 223–235 (2016).
18. Liu, C. C. & Maciel, G. E. The fumed silica surface: a study by NMR. *J. Am. Ceram. Soc.* **118**, 5103–5119 (1996).
19. Komarneni, S. et al. 27Al and29Si magic angle spinning nuclear magnetic resonance spectroscopy of Al-substituted tobermorites. *J. Mater. Sci.* **20**, 4209–4214 (1985).
20. Cong, X. & Kirkpatrick, R. J. 29Si MAS NMR study of the structure of calcium silicate hydrate. *Adv. Cem. Based Mater.* **3**, 144–156 (1996).
21. Grangeon, S. et al. Quantitative X-ray pair distribution function analysis of nanocrystalline calcium silicate hydrates: a contribution to the understanding of cement chemistry. *J. Appl. Crystallogr.* **50**, 14–21 (2017).
22. Marty, N. C. M., Grangeon, S., Warmont, F. & Lerouge, C. Alteration of nanocrystalline calcium silicate hydrate (C-S-H) at pH 9.2 and room temperature: a combined mineralogical and chemical study. *Mineral. Mag.* **79**, 437–458 (2015).
23. Trapote-Barreira, A., Cama, J. & Soler, J. M. Dissolution kinetics of C–S–H gel: flow-through experiments. *Phys. Chem. Earth* **70-71**, 17–31 (2014).
24. Walker, C. S., Sutou, S., Oda, C., Mihara, M. & Honda, A. Calcium silicate hydrate (C-S-H) gel solubility data and a discrete solid phase model at 25°C based on two binary non-ideal solid solutions. *Cem. Concr. Res.* **79**, 1–30 (2016).
25. Miyata, S. Anion-exchange properties of hydrotalcite-like compounds. *Clays Clay Min.* **31**, 305–311 (1983).
26. Parker, L. M., Milestone, N. B. & Newman, R. H. The use of hydrotalcite as an anion absorbent. *Ind. Eng. Chem. Res.* **34**, 1196–1202 (1995).
27. Jobbágy, M. & Regazzoni, A. E. Dissolution of nano-size Mg–Al–Cl hydrotalcite in aqueous media. *Appl. Clay Sci.* **51**, 366–369 (2011).
28. Xu, S. et al. Surface modification and dissolution behavior of Mg–Al hydrotalcite particles. *J. Taiwan Inst. Chem. Eng.* **56**, 174–180 (2015).
29. Hadi, J., Tournassat, C., Ignatiadis, I., Greneche, J. M. & Charlet, L. Modelling CEC variations versus structural iron reduction levels in dioctahedral smectites. Existing approaches, new data and model refinements. *J. Colloid Interface Sci.* **407**, 397–409 (2013).
30. Gran, G. Determination of the equivalence point in potentiometric titrations. Part II. *Analyst* **77**, 661–671 (1952).
31. Agnel, M. I. et al. Mechanistic and thermodynamic insights into anion exchange by green rust. *Environ. Sci. Technol.* **54**, 851–861 (2020).
32. Grangeon, S. et al. In-situ determination of the kinetics and mechanisms of nickel adsorption by nanocrystalline vernadite. *Chem. Geol.* **459**, 24–31 (2017).
33. Grangeon, S., Marty, N. C. M., Maubec, N., Warmont, F. & Claret, F. Selenate sorption by hydrated calcium aluminate (AFm): evidence for sorption reversibility and implication for the modeling of anion retention. *ACS Earth Space Chem.* **4**, 229–240 (2020).
34. Doebelin, N. & Kleeberg, R. Profex: a graphical user interface for the Rietveld refinement program BGMN. *J. Appl. Crystallogr.* **48**, 1573–1580 (2015).
35. Grangeon, S. et al. On the nature of structural disorder in calcium silicate hydrates with a calcium/silicon ratio similar to tobermorite. *Cem. Concr. Res.* **52**, 31–37 (2013).
36. Ounsy, M., Girardot, R., Saintin, K. & Viguier, G. Online data reduction for high throughput beamlines. in *International Conference on Accelerators and Large Experimental Physics Control Systems*, *San Francisco, USA, October 6-11*. (Lawrence Livermore National Laboratory, 2013).
37. Juhas, P., Davis, T., Farrow, C. L. & Billinge, S. J. L. PDFgetX3: a rapid and highly automatable program for processing powder diffraction data into total scattering pair distribution functions. *J. Appl. Crystallogr.* **46**, 560–566 (2013).
38. Massiot, D. et al. Modelling one- and two-dimensional solid-state NMR spectra. *Magn. Reson. Chem.* **40**, 70–76 (2002).
39. Marty, N. C. M. et al. Dissolution kinetics of synthetic Na-smectite. An integrated experimental approach. *Geochim. Cosmochim. Acta* **75**, 5849–5864 (2011).
40. Marty, N. C. M. et al. Weathering of an argillaceous rock in the presence of atmospheric conditions: a flow-through experiment and modelling study. *Appl. Geochem.* **96**, 252–263 (2018).
41. Parkhurst, D. L. & Appelo, C. Description of input and examples for PHREEQC version 3—a computer program for speciation, batch-reaction, one-dimensional transport, and inverse geochemical calculations. *US Geol. Surv. Tech. Methods* **6**, 497 (2013).
42. Giffaut, E. et al. Andra thermodynamic database for performance assessment: ThermoChimie. *Appl. Geochem.* **49**, 225–236 (2014).
43. Tournassat, C. et al. Cation exchange selectivity coefficient values on smectite and mixed-layer illite/smectite minerals. *Soil Sci. Soc. Am. J.* **73**, 928–942 (2009)

Acknowledgements

SOLEIL data were acquired in the frame of proposal 20201725. This study was funded by a research project (VERMEA) that takes place in the frame of an Andra/BRGM scientific partnership. Financial support from the IR

INFRANALYTICS FR2054 for conducting the research is gratefully acknowledged.

Author contributions

S.G.: methodology, formal analysis, investigation, writing, visualization. M.D.: conceptualization, investigation, resources, writing, supervision, project administration, funding acquisition. V.M.: formal analysis, investigation, writing, visualization. E.K.: investigation, writing. C.L.: formal analysis, investigation, visualization. N.Ma.: investigation. N.Mi.: conceptualization, resources, formal analysis, writing, project administration, funding acquisition. X.B.: conceptualization, resources, formal analysis, writing, project administration, funding acquisition. C.M.: conceptualization, resources, formal analysis, writing, project administration, funding acquisition. B.C.: conceptualization, resources, formal analysis, editing. N.M.: methodology, software, formal analysis, investigation, writing, visualization. All authors read and approved the final manuscript.

Competing interests

The authors declare no competing interests.

Additional information

Supplementary information The online version contains supplementary material available at https://doi.org/10.1038/s41529-024-00488-0.

Correspondence and requests for materials should be addressed to Sylvain Grangeon or Mathieu Debure.